Experimental Thermal and Fluid Science 46 (2013) 1–7

Contents lists available at SciVerse ScienceDirect

Experimental Thermal and Fluid Science

journal homepage: www.elsevier.com/locate/etfs

The flow field and axial thrust generated by a rotating rigid helix at low Reynolds numbers

Shan Zhong [a,*], Keith W. Moored [b], Victor Pinedo [b], Jesus Garcia-Gonzalez [a], Alexander J. Smits [b]

[a] School of Mechanical, Aerospace and Civil Engineering, University of Manchester, UK
[b] Department of Mechanical and Aerospace Engineering, Princeton University, Princeton, NJ 08544, USA

ARTICLE INFO

Article history:
Received 6 May 2012
Received in revised form 28 August 2012
Accepted 29 October 2012
Available online 29 November 2012

Keywords:
Bio-fluids
Locomotion
Rotating helices
Low-Reynolds number flow

ABSTRACT

Here we report an experimental study of the flow field and axial thrust generated by a single rigid helix rotating around its axis at Reynolds numbers based on the tangential velocity and the helix diameter between 0.045 and 0.18. Particle image velocimetry measurements are carried out on helices with pitch angles of 30°, 45° and 60°, at three different rotating frequencies. It is demonstrated that the helix produces a helical flow pattern about its axis that is 180° out of phase to the shape of the helix. An axial flow is generated which is in the opposite direction to the thrust produced by the helix. At a fixed pitch angle, the magnitude of this axial velocity increases linearly with the frequency of rotation, whereas at a fixed frequency the helix with a pitch angle of 45° produces the highest axial velocity. The same trend is observed in the axial thrust, which is measured using a force sensor. The measured thrust coefficient is compared with the thrust coefficient predicted by resistive-force theory. The thrust coefficient agrees well with that predicted by resistive-force theory for lower pitch angles, but resistive-force theory breaks down for pitch angles <45°, which is attributed to hydrodynamic interactions among helical loops at higher pitch angles.

1. Introduction

Micro-organisms, such as bacteria and spermatozoa, range from a few hundred nanometers to a few hundred microns in length and swim at velocities ranging from ten to a few hundred microns per second. Their typical Reynolds number for swimming is in a regime where viscous forces dominate. To propel themselves in this low Reynolds number environment, some micro-organisms propagate helical waves down their flagella from head-to-tail producing a net viscous thrust force in the opposite direction [1,2].

When a section of a helix-shaped flagellum moves through the fluid obliquely, due to the rotation of the helix and the pitch angle of the helix, it experiences forces normal and tangential to the helical segment that oppose the motion (Fig. 1c). Since the magnitude of the normal force coefficient is larger than that of the tangential force coefficient, for long thin filaments at low Reynolds number, there is a larger force normal to the helical segment than tangential. When the segment force contributions are integrated along the length of the helix, the result is a net thrust force acting on the helix in a direction opposite to the wave propagation.

The propulsion of micro-organisms by flagellar motions has been a subject of considerable interest, especially in the period from the 1950s to the 1970s when slender-body theory for Stokes flow was developed (see, for example, [3–5]). In slender-body theory, the flow field is solved by finding the distributions of Stokelets and dipoles along the center-line of the flagellum that satisfy the velocity boundary conditions on the flagellar surface. In particular, Gray and Hancock [6] developed relationships for the normal and tangential coefficients of viscous resistance acting on a long thin cylindrical filament moving through a viscous fluid. This forms the foundation of the widely-adopted resistive-force theory, which provides a simple analytical method for calculating the swimming speed and thrust produced by flagellar motions [7].

A renewed interest in low Reynolds-number propulsion has emerged in recent years due to the growing attention to biomimetics that has opened up the prospect of many new bio-robotic applications. In the context of micro-swimmers, Dreyfus et al. [8], Roper et al. [9], and Gauer and Stark [10] have studied swimmers that are propelled by a linear chain of colloidal magnetic particles linked by DNA, which exhibits a beating pattern when it is driven by an oscillating external magnetic field. These devices, for example, could be used to transfer a red blood cell to a designated location. In contrast, the artificial swimmer proposed by Edd et al. [11] is a surgical micro-robot propelled by rotating helical tails that could swim inside the human ureter to destroy kidney stones non-invasively.

The development of effective devices of this kind will require a better understanding of propulsion at very low Reynolds

* Corresponding author. Tel.: +44 161 2754318.
E-mail address: shan.zhong@manchester.ac.uk (S. Zhong).

0894-1777/$ - see front matter © 2012 Elsevier Inc. All rights reserved.
http://dx.doi.org/10.1016/j.expthermflusci.2012.10.019

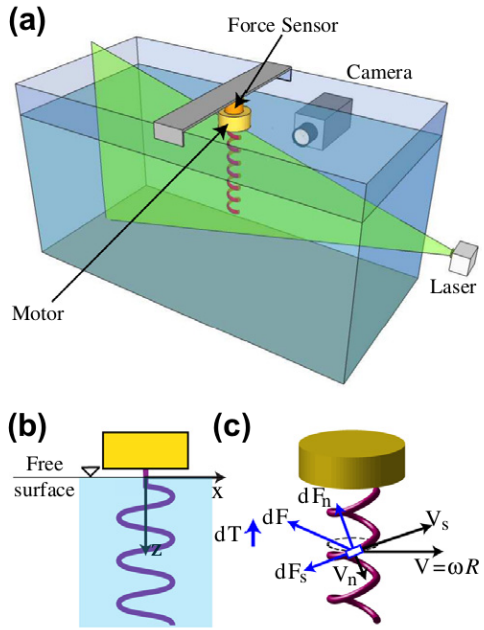

Fig. 1. (a) Apparatus and PIV setup. (b) Helix coordinate system. (c) Kinematics of and forces acting on a helix segment. The velocity of the segment is V, where $\omega = 2\pi f$, f is the frequency of rotation and R is the helix radius. The velocity can be decomposed into a tangential velocity, V_s, and normal velocity, V_n. The force contribution from the segment, dF, is decomposed into a tangential force component, dF_s, and a normal force component, dF_n. The contribution to the thrust from the segment is dT.

numbers, and yet the number of experimental studies of low Reynolds number propulsion is limited. Although it is possible to study live animals microscopically [6,12,13], experiments are often conducted on macro-scale models in a highly viscous fluid to avoid the difficulties in measuring the flow around microscopic structures. For example, Behham and Sitti [14] measured the thrust force produced by a rotating rigid helix, which was fixed to a stationary frame in a silicone oil bath, and Kim et al. [15] performed Particle Image Velocimetry (PIV) measurements of the flow field induced by two rigid helices as well as a bundling flexible helix pair. However, to the best of our knowledge, a more complete experimental data set on the velocity field generated by a single rotating helix has not yet been presented, and a critical assessment of resistive-force theory using experimental data is also lacking.

Here we report the results obtained from experiments on a macro-scale model of a single rigid helix rotating around its axis in a highly viscous fluid at low Reynolds numbers. The flow field around a helix with three different pitch angles was measured using PIV at three different helix rotating frequencies. The thrust produced by the rotating helix with seven different pitch angles was also measured using a force sensor and the results were compared with the thrust predicted from resistive-force theory.

2. Experimental setup

The helices used in the present work are left-handed helices since the flagella of most micro-organisms are left-handed. The helices have a radius of $R = 8.5$ mm and an axial length of $L = 220$ mm, and they were made by wrapping 2 mm diameter copper wire around a mandrel. The helical diameter was chosen such that the models have a diameter to axial length ratio close to the typical value of *Escherichia coli* bacteria [16] while ensuring a convenient size for the experiment. The three helices used in the PIV measurements have a pitch angle of $\beta = 30°$, 45° and 60°, corresponding to a helical pitch of $\lambda = 93$, 53 and 31 mm, respectively, with the relationship between them given by

$$\tan\beta = \frac{2\pi}{\lambda}R, \tag{1}$$

To investigate the thrust production, helices with seven different pitch angles ranging from 15° to 67° were also tested. To minimize the end effects, the axial length of the models was chosen to allow more than one complete helical pitch length for the helix of 15° pitch angle, which has the longest pitch.

The experiment was performed in a rectangular tank measuring 600 mm by 300 mm in cross-section, with a depth of 400 mm (Fig. 1a). The working fluid was silicone oil with a density of 975 kg/m^3 and a dynamic viscosity of 5 Pa s. The helix was mounted vertically, and attached to the shaft of a Faulhaber micro gear motor that has a maximum rotational frequency of 4 Hz and a maximum continuous torque of 23 mN m.

Great care was taken to align the axis of the helix with the shaft of the motor. An ATI multi-axis force sensor with a resolution of 1.6 mN was used to measure the thrust, which was sampled at 100 Hz, and averaged over at least ten rotation cycles of the helix. The torque produced by the rotating helix was too small to be measured by this sensor.

During the PIV experiment, each helix was rotated at frequencies of $f = 0.25$, 0.5 and 1 Hz. The lowest frequency is set by the smallest thrust that the force sensor can measure with acceptable accuracy, and the highest frequency is set by the camera frame rate, which determines the time interval between consecutive PIV images.

The Reynolds number, Re, based on the tangential velocity and the diameter of the helix ranged from 0.045 to 0.18. In this range it is unclear whether the Stokes flow assumption is valid and these Reynolds numbers are considerably larger than the values typical of bacteria and spermatozoa. Yet, we found that the magnitude of the average momentum flux was always two orders of magnitude smaller than the measured thrust force, which ranges between 5 and 43 mN. Hence the inertial term makes a negligible contribution to the generation of thrust, confirming that the Stokes flow assumption is valid and the results presented here will apply to lower Reynolds numbers typical of many micro-organisms. Furthermore, the range of Reynolds number studied in this experiment is close to the Reynolds number at which medical microrobots are likely to operate.

The PIV measurements were made on the central plane that bisects the helix. The experimental setup is shown in Fig. 1. Hollow glass spheres with a typical diameter of 23 μm were used as the PIV seeding. Due to their extremely long settling time in silicone oil, the necessary level of seeding density was easily maintained. The laser sheet was produced by a 5 W Spectra-Physics Argon-ion laser, and the images were taken at 30 frames per second using a Sony HDR-SR10 video camera, which has a 5 mm optical sensor and a resolution of 1920 × 1080 pixels.

The velocity vector fields were obtained by cross-correlating consecutive image pairs in the video sequence. The images were processed using PIV software developed in house with a 16 × 16 pixel interrogation area and 50% overlap [17]. The viewing area was chosen to be 190 × 106 mm and it intersects the middle portion of the helix, which is 220 mm in length. The spatial resolution of the measurement is 0.79 mm in both the vertical and horizontal directions. The rms velocity measurement error was found to be 0.17 mm/s by using the error analysis method described by Kim et al. [15], and it is small in comparison with the typical velocity of 10 mm/s measured in the flow field.

To reduce the noise levels, the velocity field data were phase-averaged. Because the video recording frequency was fixed at 30 Hz, the number of phases obtained in a cycle varied with the

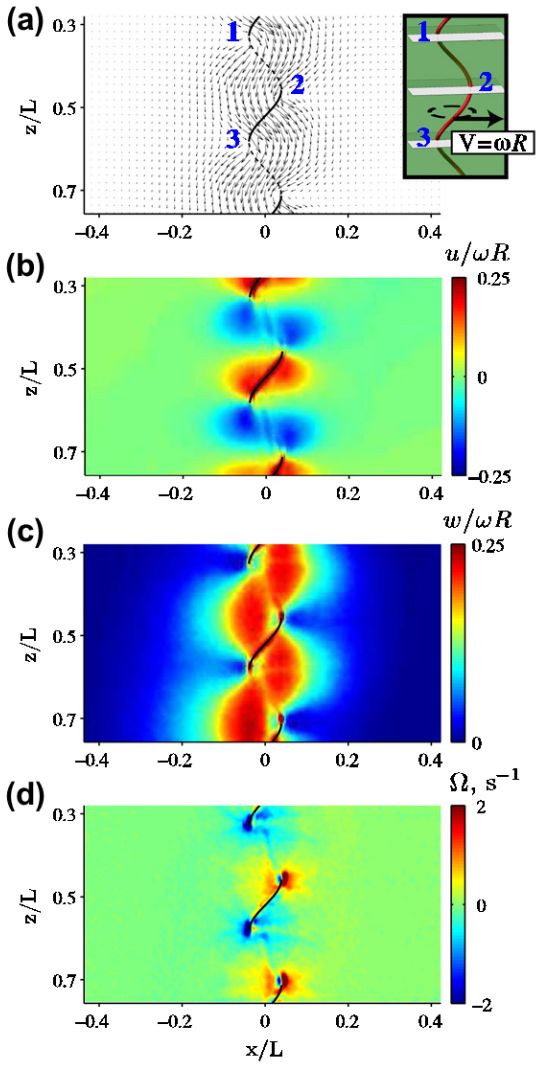

Fig. 2. Phase-averaged PIV results of a 45° helix rotating at 0.5 Hz: (a) Velocity vector field, (b) contours of normalized transverse velocity, (c) contours of normalized axial velocity and (d) contours of vorticity.

frequency of rotation of the helix with a total of 120, 60 and 30 phases available for a helix rotating at a frequency of 0.25, 0.5 and 1 Hz respectively. It was found that the smoothness of the velocity contours was improved when the number of cycles used in the phase-averaging was increased from 25 to 50, but no further improvement was noted by going from 50 to 100. For all the results presented here 100 cycles of data were used in order to produce smoother vorticity contours.

3. Characteristics of the flow field

A typical phase-averaged velocity vector field on the central plane of the 45° helix rotating at 0.5 Hz is shown in Fig. 2a. The shape of the helix at the corresponding instant is also shown to assist the interpretation of the flow field. The x and z axes have their origin at the free surface with the positive z axis in the vertical downward direction (Fig. 1b). In the PIV image, the laser sheet is directed from left to right and intersects the helix at this instant at Points 1, 2 and 3. The helix is left-handed and rotates in the anti-clockwise direction to generate a helical wave propagating downwards. Points 1 and 3 are moving out of the page whereas Point 2 is moving into the page (see the accompanying three-dimensional drawing in Fig. 2a). The helix segment 2–3 is in front of the laser sheet and is moving to the right. As this segment moves to the right, there is a resultant force dF produced, acting on the helix segment (Fig. 1c). There is an equal and opposite force acting on the fluid that causes the fluid to move to the right and downward, as indicated by the velocity vectors (Fig. 2a). As the force acting on the helix increases (and thus the force acting on the fluid), it is expected that the velocity induced by the helix also increases, which will be shown later to indeed be the case.

In contrast to segment 2–3, the helix segment 1–2 is behind the laser sheet. It is moving to the left and drags the flow to the left and downward. The three-dimensional pattern that arises is a helical flow that is 180° out of phase to the shape of the helix (Fig. 2a). The alternating left and right motion of the fluid generated by the rotating helix is also illustrated in the contours of transverse velocity shown in Fig. 2b. The corresponding axial velocity contours displayed in Fig. 2c clearly demonstrate the downward motion of the fluid generated by the rotating helix. In Fig. 2 the velocity is normalized by the corresponding tangential velocity of the rotating helix, ωR, where $\omega = 2\pi f$.

There is a concentration of vorticity at the intersection points of the helix with the laser sheet where the most abrupt flow turning takes place (Fig. 2d). The vorticity is negative at Points 1 and 3 and positive at Point 2, in accordance with the direction of flow turning. A small region with a discontinuity in vorticity to the right of these points is visible, which is caused by a blockage of laser light by the helix. The velocity and the vorticity fields exhibit similar features as those observed by Kim et al. [15] in their study of a pair of interacting helices.

The normalized axial velocity fields produced by the 45° helix rotating at the three different frequencies are shown in Fig. 3.

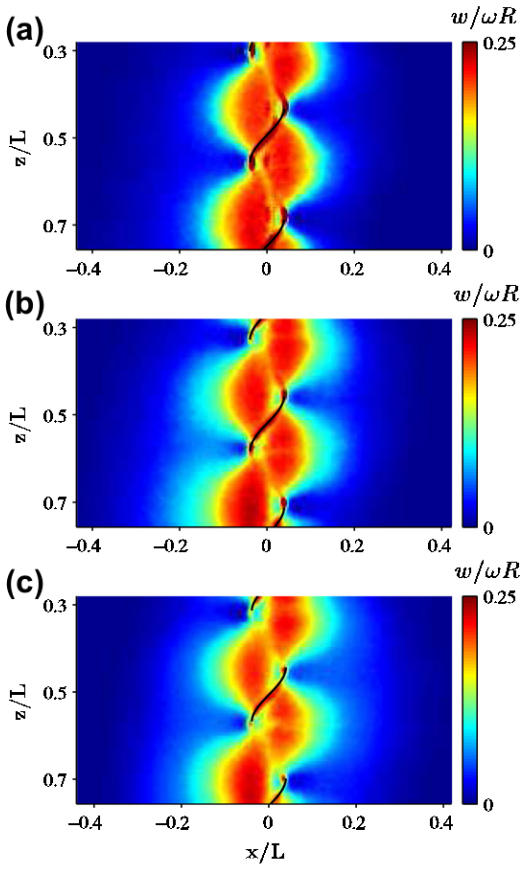

Fig. 3. Contours of normalized phase-averaged axial velocity for the 45° helix rotating at a frequency of (a) 0.25 Hz, (b) 0.5 Hz and (c) 1 Hz.

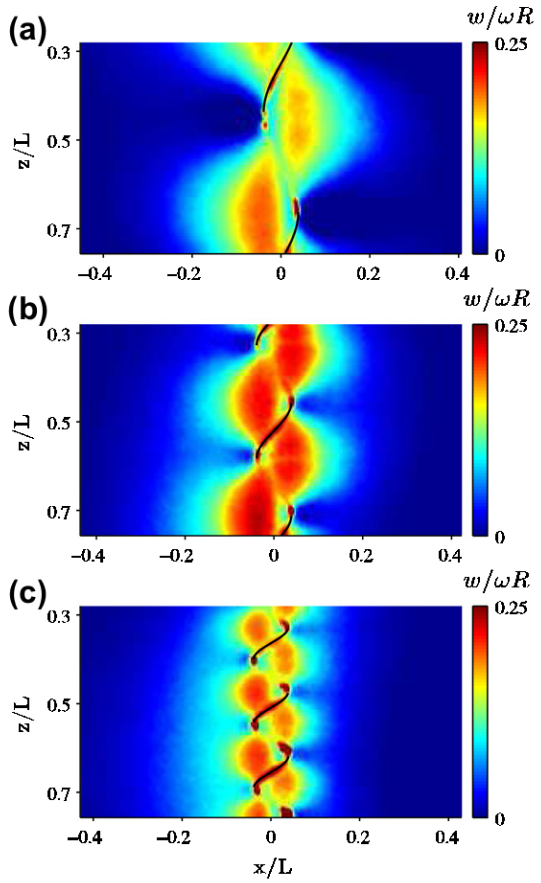

Fig. 4. Contours of normalized phase-averaged axial velocity of a helix rotating at a frequency of 0.5 Hz with a pitch angle of (a) 30°, (b) 45° and (c) 60°.

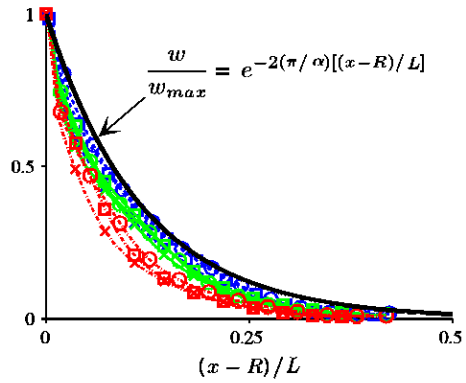

Fig. 5. Decay of axial velocity as a function of $(x-R)/L$. An exponential variation (solid line) is shown for comparison using $\alpha = 0.74$ as suggested by Shen and Arritia [18] for Newtonian flows. The red dash-dot lines denote $f = 0.25$ Hz, the green solid lines denote $f = 0.5$ Hz, and the blue dashed lines denote $f = 1$ Hz. The o marks represent a pitch angle of 30°, while the square marks represent a pitch angle of 45° and the x marks represent a pitch angle of 60°. (For interpretation of the references to colour in this figure legend, the reader is referred to the web version of this article.)

The similarity in the flow pattern at different frequencies implies that the magnitude of the axial velocity increases proportionally with an increasing rotational frequency, which is consistent with resistive-force theory.

The axial velocity fields produced by the helices with three different pitch angles rotating at 0.5 Hz are shown in Fig. 4. As expected, a helix with a higher pitch angle produces a spatially more frequent turning of the fluid along a given axial length. Nevertheless, the 45° helix appears to produce the strongest axial velocity.

Fig. 5 shows the normalized axial velocity of the fluid flow w/w_{max} as a function of the normalized distance $(x-R)/L$ away from the helix in the x-direction. The maximum axial velocity occurs at the radius of the helix and is denoted as w_{max}. The curves are obtained by ensemble-averaging the velocity profile as a function of $(x-R)/L$ along the section of the helix located within the PIV measurement area and over one rotation cycle. These data lead to three observations. First, the velocity appears to exhibit an approximate exponential decay of the form previously obtained by Lighthill [4]. Here, an α value of 0.74 is used for producing the exponential velocity decay for Newtonian flows [18]. By comparison, the helical case shows a faster velocity decay rate which is likely to be related to three-dimensionality of the helical flow whereas the flow produced by Lighthill's undulating sheet is essentially two-dimensional. Second, the velocity decay profiles almost collapse onto a single curve at $f = 0.5$ and 1 Hz for the three helical pitches. The departure of the velocity decay profiles at $f = 0.25$ Hz from those of the higher frequencies is likely to be caused by the relatively higher uncertainties in the PIV measurements due to the very low velocities in the regions far away from the helix. Finally, the velocity appears to decay rapidly such that it is reduced to less than 5% of the maximum velocity within less than 30% of the body length. In the present experiment, the walls of the rectangular tank are located away from the centerline of the helix by 300 mm (1.36L) or 150 mm (0.68L), depending on the direction. It would appear, therefore, that the presence of the walls has a negligible effect on the flow field around the helix.

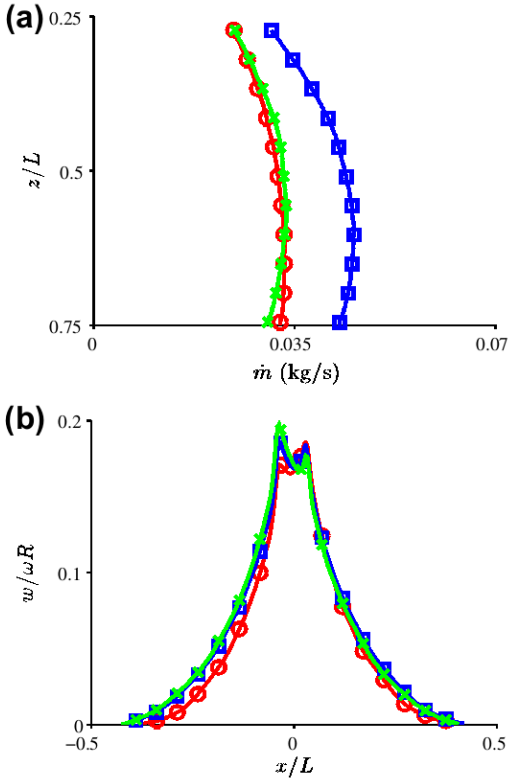

Fig. 6. (a) Variations of mass flux along the helix. The red o-marked line denotes $\beta = 30°$, the blue square-marked line denotes $\beta = 45°$ and the green x-marked line denotes $\beta = 60°$. (b) Axial velocity distributions at three different streamwise locations for the helix with $\beta = 45°$. The red o-marked line denotes $z/L = 0.32$, the blue square-marked line denotes $z/L = 0.52$ and the green x-marked line denotes $z/L = 0.72$. (For interpretation of the references to colour in this figure legend, the reader is referred to the web version of this article.)

As shown in Figs. 3 and 4, the rotating helix generates a downward velocity, which transports fluid in the opposite direction to the thrust acting on the helix. Fluid transport at low Reynolds numbers is an important phenomenon seen throughout biology [19,20]. To characterize the fluid mass transport as a function of the pitch angle and the frequency of motion, the mass flux, $\dot{m}$, through the plane normal to the helical axis is calculated from the PIV data. The variation in mass flux along the length of the helix for $\beta = 30°$, 45° and 60° at $f = 1$ Hz are shown in Fig. 6a. At a given pitch angle, the streamwise mass flux peaks at a downstream location around $z/L \approx 0.6$ with lower mass flux at $z/L = 0.25$ and 0.75. The cause for the lower mass flux at these locations is presumably end effect flow corrections near the free-surface and near the helix tail. At the free-surface the mass flux must necessarily go to zero while at the tail of the helix the external fluid forcing must go to zero. It can also be seen that the mass flux is maximized at a pitch angle of 45°, which is consistent with the observation that the axial velocity also reaches a maximum at this pitch angle (Fig. 4).

What is important to note is that end effects do play a role on the generated flow fields and that the no flux condition alters the flow more substantially than the no forcing condition. However, as shown in Fig. 6a, the length of helix that is affected by each end effect appears to be the same, regardless of the pitch angle tested. This is expected since the extent of the flow field that is affected by the end conditions should be strongly dependent on the length-to-diameter ratio of the helix. This point is important for the later comparison between resistive-force theory and the experiments.

The time-averaged axial velocity profiles (Fig. 6b) over a rotation cycle of the helix with $\beta = 45°$ at three streamwise locations reveal that the increase in the mass flux from $z/L = 0.32$ to 0.52 is correlated to a slight widening of the streamwise flow region. Due to mass conservation the flow is turned from the cross-stream direction (near the free-surface) to the streamwise direction (near the middle of the helix). Until the flow is fully turned, the velocity profiles will be narrower reflecting the lower mass flux in the streamwise direction.

4. Comparison between measured and predicted thrust

To compare the experimentally measured thrust with resistive-force theory, we note that the underlying assumption of the theory is that the hydrodynamic forces are proportional to the local body velocity, with the constant of proportionality being defined by the coefficient of resistance. Consider a long thin cylindrical filament that is in motion through a viscous fluid (Fig. 1c). If the tangential and normal velocities of a cylindrical element of length ds are V_s and V_n respectively, the tangential and normal forces are given by

$$\begin{aligned} dF_s &= -C_s V_s\, ds, \\ dF_n &= -C_n V_n\, ds, \end{aligned} \tag{2}$$

where C_s and C_n are the corresponding coefficients of resistance.

The expressions for C_s and C_n given by Gray and Hancock [6] are frequently used, where

$$\begin{aligned} C_s &= \frac{2\pi\mu}{\ln(2\lambda/b) - 0.5}, \\ C_n &= 2C_s. \end{aligned} \tag{3}$$

The radius of the element is b and the dynamic viscosity of the fluid is μ. Cox [21] and Johnson and Brokaw [22] suggested instead

$$\begin{aligned} C_s &= \frac{2\pi\mu}{\ln(2\lambda/b) - 0.5}, \\ C_n &= \frac{4\pi\mu}{\ln(2\lambda/b) + 0.5}. \end{aligned} \tag{4}$$

For a rotating helix which does not translate in the fluid

$$\begin{aligned} V_s &= \omega R \sin\beta, \\ V_n &= \omega R \cos\beta. \end{aligned} \tag{5}$$

The pitch angle β is related to λ and R via Eq. (1). Finally, the propulsive force acting along the axial direction of the helix on a cylindrical element of length ds is given by

$$dF = dF_n \sin\beta - dF_s \cos\beta. \tag{6}$$

The total thrust produced by the helix can then be found by integrating the force acting on each element along the helix. Hence,

$$F = \int_0^S \omega R (C_n - C_s) \sin\beta \cos\beta\, ds. \tag{7}$$

so that for a fixed S,

$$F = \frac{1}{2}\omega R S (C_n - C_s) \sin 2\beta, \tag{8}$$

and for a fixed L,

$$F = \omega R L (C_n - C_s) \sin\beta, \tag{9}$$

where L is the axial length of the helix and S is the length of the helix when it is straightened.

Eqs. (8) and (9) indicate that the thrust produced by a helix of given geometry is linearly proportional to its rotational frequency, its radius, its length, and the fluid viscosity, which is contained in the coefficients of resistance. This equation also indicates that the thrust is affected by the pitch angle, β, in a more intricate manner since $(C_n - C_s)$ is a function of the pitch angle as well.

In the present experiment, L is fixed. The thrust measurements were carried out on helices of seven different pitch angles ranging from 15° to 67° and rotating at eight different frequencies from 0.25 to 2 Hz with an increment of 0.25 Hz. Fig. 7 shows the thrust force as a function of rotational frequency for each pitch angle. It is clear that there is a linear relationship between the rotational frequency and the force produced; supporting the underlying assumption of resistance force theory.

The results of all thrust measurements are shown in Fig. 8. Here the thrust is non-dimensionalized by $\mu\omega R\, L$, which allows the data obtained at different rotating frequencies and slightly different lengths to collapse. Sixteen data points are shown at each pitch angle with the two different symbols representing the data acquired from two separate sets of tests. The variation in the data at a given pitch angle is representative of the uncertainty in the thrust measurements. A clear maximum in the measured thrust coefficient near $\beta = 45°$ is observed, which matches the trend seen earlier in the axial velocity.

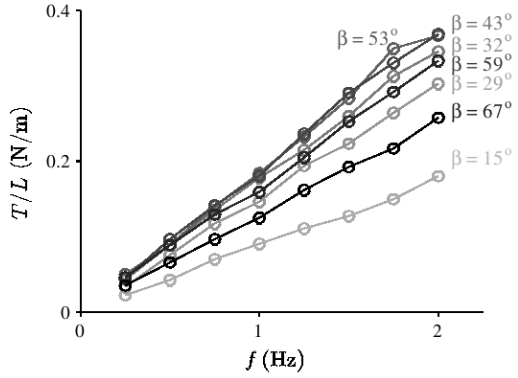

Fig. 7. Direct thrust per unit length measurements as a function of the frequency of rotation.

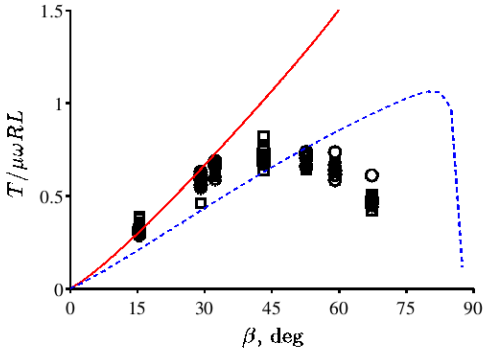

Fig. 8. A comparison of the thrust coefficients from experimental measurements (points) and from resistive-force theory (lines). The solid line is calculated using Eq. (3) while the dashed line is calculated using Eq. (4). The experimental data points were measured over a frequency range of $0.25 \leqslant f \leqslant 2$ Hz. The squares and circles represent two different experimental data sets.

The thrust force calculated from resistive-force theory (Eq. (9)) is also shown for comparison, using both sets of coefficients of resistance (Eqs. (3 and 4)). In contrast to the experiments, the theoretical thrust coefficient is found to increase monotonically with β until $\beta = 89°$ and 80°, respectively, before it decreases sharply to zero at $\beta = 90°$. Nevertheless, the theoretical thrust coefficient appears to follow the experimental values up to $\beta = 45°$ before the deviation becomes significant. Both sets of coefficients perform reasonably well when $\beta < 45°$, which is evident from the fact that the experimental data lies between the two theoretical thrust coefficient curves in this range. However, the coefficients given by Eq. (4) outperform those given by Eq. (3) at $\beta > 45°$.

For a helix of a fixed diameter, deviation from the predictions of resistive-force theory may be caused by two factors not accounted for in the theory: hydrodynamic interactions among helical loops, and/or end effects. The importance of hydrodynamic interactions should increase as the pitch angle is increased (that is, as the helical loops get closer to each other). The importance of end effects should increase as the length-to-diameter ratio of the helix becomes smaller. However, the importance of end effects should not vary significantly with the pitch angle if the length-to-diameter of the helix is held constant as seen in Fig. 6a. Since the deviation between the theoretical predictions and the experiments occurs due to variations in pitch angle while the length-to-diameter ratio is fixed, we attribute this deviation to hydrodynamic interactions among helical loops that are unaccounted for in resistive-force theory. In fact, at lower pitch angles ($\beta \leqslant 45°$) there is good agreement between resistive-force theory and the experiments and as the pitch angle is increased the same proportion of the helix is affected by the end conditions. These two points imply that the end conditions have a small effect on the thrust production for all of the pitch angles at this length-to-diameter ratio.

Highlighting the limitations of resistive-force theory is not unprecedented. Johnson and Brokaw [22] were the first to show that the lack of hydrodynamic interactions in resistive-force theory leads to a discrepancy with the more accurate computations of slender-body theory for the case when a cell-body of a significant size was attached to an undulating flagellum. Jung et al. [23] has also attributed discrepancies between their helix towing experiments and resistive-force theory to the omission of hydrodynamic interactions.

5. Conclusions

Based on PIV results obtained from a rotating rigid helix with a pitch angle of $\beta = 30°$, 45° and 60°, it was shown that the flow field generated by the helix displays a helical flow pattern about its axis, which is 180° out of phase with the shape of the helix. The helix also generates an axial flow in the opposite direction of the thrust acting on the helix, due to an equal and opposite force acting on the fluid. The axial velocity increases linearly with the rotating frequency, and at a fixed frequency the helix with a pitch angle of 45° produces the highest axial velocity of the three helices tested here. This trend mirrors the trend in thrust measured using a force sensor, which shows a clear maximum when the pitch angle of the helix is at $\beta = 45°$. The trend in the thrust force, however, deviates from the predictions of resistive-force theory for helices of a fixed axial length. Resistive-force theory yields a monotonic increase in thrust up to a much higher pitch angle of nearly $\beta = 90°$. The discrepancy is attributed to hydrodynamic interactions that are not accounted for in resistive-force theory, which become more significant as helical loops become more closely packed at higher pitch angles for a fixed length-to-diameter ratio. In future work, numerical simulations of the flow field generated by a rigid rotating helix will be compared with the predictions from resistive-force theory so as to provide further insight.

Acknowledgements

The authors would like to gratefully acknowledge the support of the National Science Foundation, Grant DBI 1062052. Also, the first author, Shan Zhong, would like to acknowledge the financial support from the Leverhulme Trust in the UK, which allowed to her to undertake this work at Princeton University during her sabbatical visit. The authors would like to thank Mr. Joseph Sivo for his time and patience in making the helix models.

References

[1] E. Purcell, Life at low Reynolds number, Amer. J. Phys. 45 (1977) 3–11.
[2] S. Vogel, Life in Moving Fluids: The Physical Biology of Flows, Princeton University Press, 1994.
[3] G.J. Hancock, The self-propulsion of microscopic organisms through liquids, Proc. Roy. Soc. London Ser. A. 217 (1953) 96–121.
[4] J. Lighthill, Flagella hydrodynamics, SIAM Review 18 (2) (1976) 161–230.
[5] J.J.L. Higdon, The hydrodynamics of flagellar propulsion: helical waves, J. Fluid Mech. 94 (1979) 331–351.
[6] J. Gray, G.J. Hancock, The propulsion of sea-urchin spermatozoa, J. Exp. Biol. 32 (1955) 802–814.
[7] A.T. Chwang, T.Y. Wu, A note on the helical movement of micro-organisms, Proc. Roy. Soc. Lond. B. 178 (1971) 327–346.
[8] R. Dreyfus, J. Baudry, M.L. Roper, M. Fermigier, H.A. Stone, J. Bibette, Microscopic artificial swimmers, Nature 437 (2005) 862–865.
[9] M. Roper, R. Dreyfus, J. Baudry, M. Fermigier, J. Bibette, H.A. Stone, On the dynamics of magnetically driven elastic filaments, J. Fluid Mech. 554 (2006) 167–190.
[10] E. Gauer, H. Stark, Numerical study of a microscopic artificial swimmer, Phys. Rev. E 74 (2006) 021907.
[11] J. Edd, S. Payen, B. Rubinsky, M.L. Stoller, M. Sitti, Biomimetic propulsion for a swimming surgical microrobot, in: Proceedings of 2004 IEEE International Conference on Intelligent Robots and System, IEEE, New York, 2004, pp. 2583–2588.
[12] L.H. Cisneros, R. Cortez, C. Dombrowski, R.E. Goldstein, J.O. Kessler, Fluid dynamics of self-propelled micro-organisms: from individuals to concentrated populations, Exp. Fluids 43 (2007). 37-753.
[13] K. Drescher, R. E Goldstein, N. Michel, M. Polin, I. Tuval, Direct measurement of the flow field around swimming microorganisms, Phys. Rev. Lett. 105 (2010) 168101.
[14] B. Behkam, N. Sitti, Modelling and testing of a biomimetic flagellar propulsion method for microscale biomedical swimming robot, in: Proceedings of the 2005 IEEE/ASME International Conference on Advanced Intelligent Mechatronics. Monterey, California, USA, 2005.
[15] M.J. Kim, M.J. Kim, J.C. Bird, J. Park, T.R. Powers, K.S. Breuer, Particle image velocimetry experiments on a macro-scale model for bacterial flagellar bundling, Exp. Fluids 37 (2004). 872-788.
[16] E. Leifson, Atlas of Bacterial Flagellation, Academic Press, New York and London, 1960.
[17] J. Jiménez, High Reynolds number flows about bodies of revolution with application to submarines and torpedoes. Ph.D. Thesis, Princeton University, Princeton, NJ, USA, 2007.

[18] X.N. Shen, P.E. Arratia, Undulatory swimming in viscoelastic fluids, Phys. Rev. Lett. 106 (2011) 208101.
[19] C. Brennen, H. Winet, Fluid mechanics of propulsion by cilia and flagella, Ann. Rev. Fluid Mech. 9 (1977) 330–398.
[20] J.L. Rosenbaum, G. Witman, Intraflagellar transport, Nat. Rev. Mol. Cell Biol. 3 (2002) 813–825.
[21] R.J. Cox, The motion of long slender bodies in a viscous fluid Part 1. General theory, J. Fluid Mech. 44 (4) (1970) 791–810.
[22] R.E. Johnson, C.J. Brokaw, Flagellar hydrodynamics: a comparison between resistive-force theory and slender-body theory, Biophys.J. 25 (1979) 113–127.
[23] S. Jung, K. Mareck, L. Fauci, M.J. Shelley, Rotational dynamics of a superhelix towed in a Stokes fluid, Phys. Fluids. 19 (10) (2007) 103–105.